Simultaneous Measurement of Humidity and Temperature Using a Hybrid Plasmonic Waveguide Bragg Grating

Zeng Wang, Guangxi Hu, Haimei Luo, Jiajia Zhao, Daixing Duan, and Wen Yuan

***Abstract*—A hybrid plasmonic waveguide Bragg grating (HPWBG) consisting of a polyvinyl alcohol (PVA) microfiber coupled with metal strips oriented at right angles is reported for simultaneous measurement of humidity and temperature. Due to the convenient adherence of PVA microfiber to metal gratings and its easy connectivity to silica fiber tapers, the hybrid plasmonic waveguide sensor exhibits high flexibility. Numerical calculation reveals that TM polarization shows more prominent Bragg reflection owing to hybrid plasmonic modes exciting. Two hybrid plasmonic TM modes, namely the fundamental mode and the high-order mode, are excited, resulting in two separate reflection peaks. As the two reflection peaks exhibit different behaviors in response to changes in humidity and temperature, simultaneous measurement of humidity and temperature can be realized through a sensitivity coefficient matrix. The experimental results show that the humidity sensitivity reaches −1.98 nm/%RH in the range of 30%–90%RH and the temperature sensitivity is −0.64 nm/°C within a temperature range of 20–90 °C for a PVA microfiber diameter of 1.57 μm. The excellent sensing performance, compactness, and flexibility of the hybrid plasmonic waveguide make it an encouraging choice for humidity and temperature sensing applications.**

***Index Terms*—Bragg gratings, optical sensors, plasmonics.**

I. Introduction

RELATIVE humidity (RH) is one of the essential environmental factors that find application in diverse domains, such as meteorological monitoring, industrial and agricultural sectors, and aerospace undertakings [1], [2], [3], [4]. As a result, there have been notable advancements in the development and utilization of humidity sensors in recent years. In comparison to conventional electronic RH sensors, fiber-optic sensors have received more attention owing to their compact size, convenient integration, cost-effectiveness, immunity to electromagnetic interference, and high resolution [5], [6], [7]. So far, various types of fiber-optic humidity sensors have been proposed [8], [9], [10], [11], [12]. Due to the sensitive characteristics towards RH and temperature, polyvinyl alcohol (PVA) has found extensive applications in the development of RH sensors based on wavelength demodulation. For example, Zhao introduced a humidity sensor based on a photonic crystal cavity, where the cavity was coated with PVA. The humidity sensitivity was 129 pm/%RH within the humidity range of 40% to 90% [13]. Shao conducted a surface plasmon resonance (SPR) sensor based on a side-polished single mode fiber coated with PVA for relative humidity sensing [14]. The sensor exhibited a high sensitivity within the relative humidity range of 40% to 90%, reaching up to 4.97 nm/%RH. In 2021, Wang conducted a study on a relative humidity sensor utilizing the SPR effect of a PVA-coated side-polished polymer fiber (POF) [15]. The sensitivity of this device was reported to be 4.98 nm/%RH within the humidity range of 30% to 90%. However, the influence of other factors on humidity measurement, such as temperature, is a critical concern. Therefore, several studies have been conducted on the simultaneous measurement of humidity and temperature. Wu proposed a temperature and humidity sensor based on an open cavity FPI sensor with PVA coating [16]. In 2023, Chen presented a sensing structure constructed by a U-shaped microfiber sensor coated with PVA nanofibers [17]. These works indicate that, through the design of fiber sensor structures, it is possible to achieve temperature and humidity dual-parameter measurement and thus eliminate cross-sensitivity.

In this article, we report a hybrid plasmonic waveguide Bragg grating (HPWBG) for simultaneous humidity and temperature measurement. The sensor consists of a PVA microfiber attached on gold gratings as a substrate. The hybrid plasmonic modes excited by coupling between the metal surface plasmon-polarition mode and PVA microfiber dielectric mode have been theoretically simulated and analyzed. Using a ∼1.57 μm-diameter PVA microfiber, a sequence of experiments was conducted encompassing fabrication as well as the tests on response to RH, temperature, and time. Detailed explanations of high sensitivity

Manuscript received 31 October 2023; revised 28 January 2024; accepted 8 February 2024. Date of publication 13 February 2024; date of current version 14 March 2024. This work was supported in part by the Training Program for Academic and Technical Leaders of Major Disciplines in Jiangxi Province under Grant 20232BCJ22012, in part by the Science and Technology Key Project of Education Department of Jiangxi Province under Grant GJJ2200306, in part by the Scientific Research Fund of Hunan Provincial Education Department of China under Grant 22B0324, and in part by the Natural Science Foundation of Hunan Province of China under Grant 2020JJ5606. *(Corresponding authors: Haimei Luo; Jiajia Zhao.)*

Zeng Wang, Guangxi Hu, Haimei Luo, Daixing Duan, and Wen Yuan are with the Jiangxi Key Laboratory of Photoelectronics and Telecommunication College of Physics and Communication Electronics, Jiangxi Normal University, Nanchang 330022, China (e-mail: 202140100625@jxnu.edu.cn; jxsdhm@jxnu.edu.cn; 202240100608@jxnu.edu.cn; 202141600149@jxnu.edu.cn; yuanwen@jxnu.edu.cn).

Jiajia Zhao is with the School of Computer and Communication Engineering, Changsha University of Science and Technology, Changsha 410114, China (e-mail: jiajiazhao@csust.edu.cn).

Digital Object Identifier 10.1109/JPHOT.2024.3365466

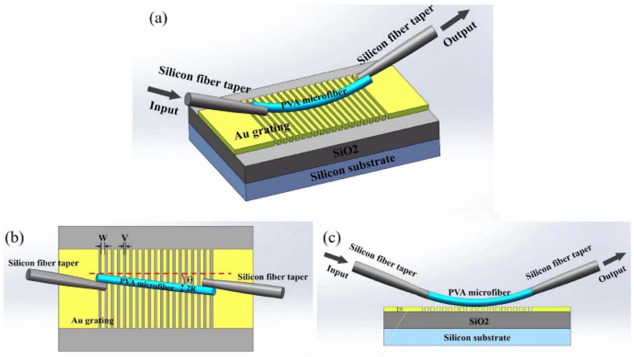

Fig. 1. Schematic illustration of the sensor structure. (a) Three-dimensional view; (b) Planar view; (c) Profile view.

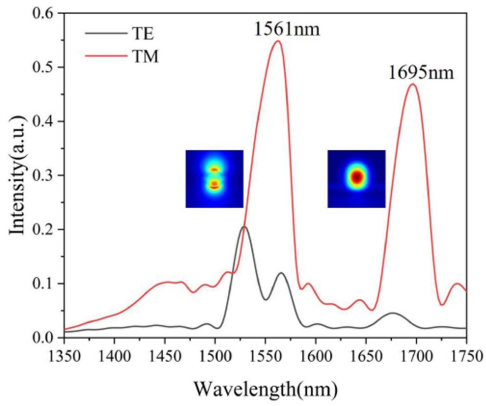

Fig. 2. Simulated reflection spectra of the HPWBG for TE and TM polarizations and the light field distribution at the reflected wavelength (1561 nm and 1695 nm) in the TM spectra.

and the ability to measure RH and temperature simultaneously will be provided in the subsequent sections.

II. Sensor Structure and Working Principle

The HPWBG structure is shown in Fig. 1. A pliable PVA microfiber is flexed to rest atop the metallic grating, which consists of an alternating arrangement of gold (Au) strips and air slots. The two ends of PVA microfibers are coupled to the waist region of the adiabatic silica single-mode fiber (SMF) tapers for input and output. The metal grating is backed by SiO_2 substrate and a silicon base is placed on the bottom layer. The width w and the height h of the metal grating are 390 nm and 500 nm, respectively, the width of the air slot is $v = 260$ nm, and the PVA microfiber's alignment angle with respect to the grating longitudinal direction is $\theta = 0°$. Therefore, the metal grating period along the PVA microfiber is $\Lambda = (w + \mathrm{v})/\cos(\theta) = 650$ nm. The diameter of the PVA microfiber and the contact length between the PVA microfiber and the metal grating are d and L, respectively.

The Bragg wavelength λ_B of the coupled system can be described as [18]

$$\lambda_B = 2n_{eff}\Lambda = 2\left(wn_{eff1} + vn_{eff2}\right) \tag{1}$$

where $n_{eff} = (wn_{eff1} + vn_{eff2})/(w + v)$, n_{eff1} and n_{eff2} correspond to the modal effective indices of the PVA microfiber with and without the presence of the metal strip, respectively. n_{eff} is dependent on the PVA microfiber diameter d. The normalized reflection spectra of the hybrid plasmonic waveguide with $d = 1.4$ μm and $L = 26$ μm for both the TM and TE polarizations are calculated by use of the three-dimensional finite-domain time-difference (FDTD) method in Fig. 2. The TM polarization is characterized as having its primary electric field oriented perpendicular to the Au film, while the TE polarization refers to the one whose primary electric field parallel to the Au film. Comparing the Bragg reflection bands of the TM and TE spectra, it can be found that the TM spectra have more obvious reflection peaks. In the following, we will concentrate on the TM mode due to its superior performance. Two distinct reflected peaks appear at the wavelengths of 1695 nm and 1561 nm in the TM spectra. The simulation results of the reflected light mode

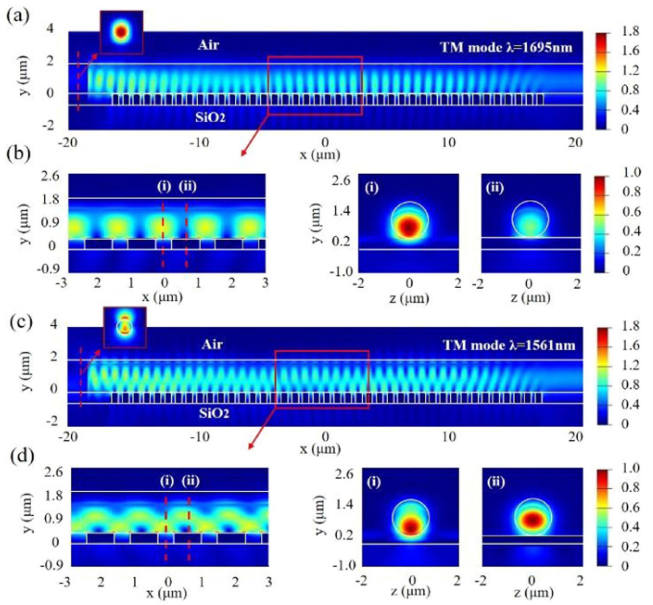

Fig. 3. (a) Calculated electric field strength evolution of light along the PVA microfiber at the wavelength of 1695 nm. Inset: the distribution of reflected light intensity in cross-sectional view. (b) Enlarged view of the area outlined by the red line in (a) and the field patterns across the dashed lines. (c) The electric field strength evolution of light at the wavelength of 1561 nm. (d) Enlarged view of the area outlined by the red line in (c).

filed distribution are shown in the inset of Fig. 2. As we can observe that the two reflected peaks are excited by different modes (the fundamental mode and the high-order mode), so that they can be used as reference dips for the simultaneously measuring humidity and temperature.

In order to gain a deeper insight into the Bragg reflection characteristics of the sensor, we conduct simulations to analyze the pattern of steady-state light electric-field intensity within the waveguide structure at the two reflective peaks shown in Fig. 3. It can be observed that on the left side of the light entering the Au grating and after leaving the metal grating, only one mode exists without interference, and a traveling wave state appears in these two regions. However, within the region of metal grating, there

is interference between two optical fields: one is the incident light field, and the other is the reflected light field caused by the metal grating. Therefore, a clear standing wave state can be observed. At a wavelength of 1695 nm, the Bragg metal grating reflection spectrum is dominated by the fundamental plasmonic mode, with the mode field mainly distributed at the center of the PVA microfiber, which is shown in Fig. 3(a) and (b). Regarding the reflection peak at a wavelength of about 1561 nm, it is formed by the high-order mode of the plasmonic mode. As we can see from Fig. 3(c) and (d) that the mode field distribution occurs at the interface between the PVA microfiber and air. When the PVA microfiber is in contact with the metal, the mode field is pushed away from the metal. Conversely, the mode field moves towards the metal when the PVA microfiber is not in contact with the metal. Due to the distinct sensitivities of these two plasmonic modes to refractive index variation and volume expansion of the PVA microfiber, the monitoring of the RH and temperature can be discriminated from each other using the coefficient matrix below [19].

$$\begin{bmatrix} \Delta T \\ \Delta RH \end{bmatrix} = \frac{1}{D} \begin{bmatrix} K_{RHh} & -K_{RHf} \\ -K_{Th} & K_{Tf} \end{bmatrix} \begin{bmatrix} \Delta\lambda_{Bf} \\ \Delta\lambda_{Bh} \end{bmatrix} \tag{2}$$

where ΔT and ΔRH are the variation of temperature and RH, respectively; $D = K_{Tf}\ K_{RHh} - K_{Th}K_{RHf}$, K_{RHf} and K_{Tf} are the RH and temperature sensitivities of the reflection peak of the fundamental mode, respectively; K_{RHh} and K_{Th} are the RH and temperature sensitivities of the reflection peak of the high-order mode, respectively; and $\Delta\lambda_{Bf}$ and $\Delta\lambda_{Bh}$ are the wavelength shifts of the reflection peak of the fundamental mode and high-order mode, respectively.

Keeping the parameters of the metal grating unchanged, we further investigate the influence of PVA microfiber diameter d, the coupling length L and the contact angle θ between PVA microfiber and metal grating on the device reflection spectrum, as illustrated in Fig. 4. Fig. 4(a) demonstrates that when the diameter increases from 1.0 μm to 1.8 μm, the short wavelength peak grows first and then gradually shrinks, while the long wavelength peak continuously decreases. Therefore, when the diameter is between 1.2 μm to 1.6 μm, the optimal reflection spectra can be obtained. Fig. 4(b) shows that the longer the coupling length, the more prominent the reflection peak and the narrower the bandwidth until it reaches saturation. Fig. 4(c) discusses the influence of the contact angle between PVA and Au gratings on sensor performance. The results indicate that the center wavelength of the reflection peak almost doesn't change, but its intensity gradually decreases with increasing contact angle.

The coupling efficiency η between 1.57 μm diameter PVA fiber and microfiber taper waist with the same diameter at room temperature is also investigated under different overlapping lengths as shown in Fig. 5(a). The reason for setting the fiber diameter to 1.57 μm is because that is the fiber diameter being tested in the experiment. The wavelength of the light is assumed to be 1550 nm and the separation of PVA fiber and silica microfiber is assumed to be zero. The results indicate that as the overlapping length increases, the coupling efficiency between silica microfiber and PVA fiber exhibits a periodic oscillation and

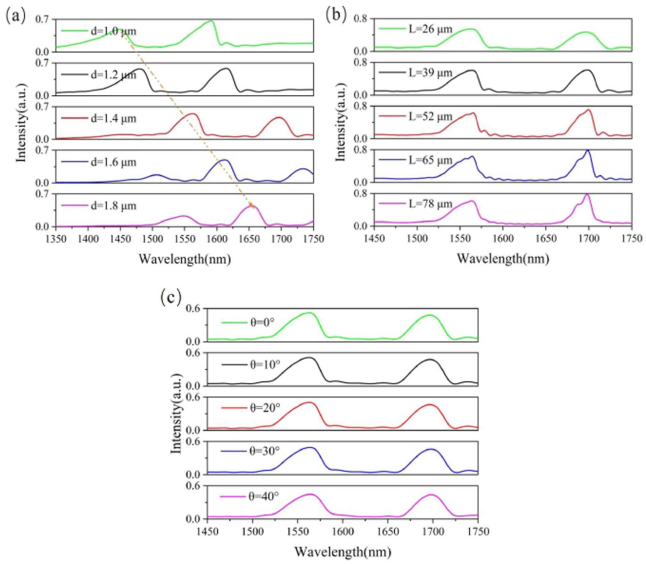

Fig. 4. Calculated reflection spectral evolution under different (a) PVA microfiber diameters (b) coupling lengths and (c) contact angles.

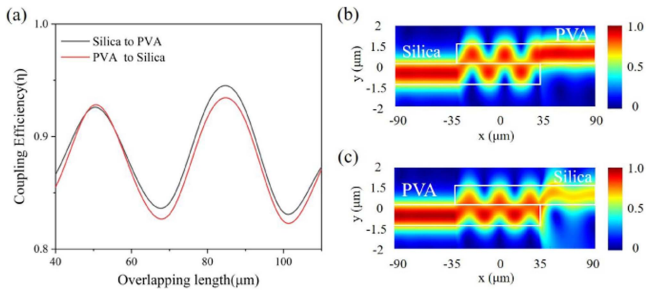

Fig. 5. (a) Coupling efficiency between silica microfiber and PVA fiber at different overlapping lengths. Power maps of light coupling from (b) silica microfiber to PVA fiber and (c) PVA fiber to silica microfiber with overlapping length of 70 μm.

fluctuates at 88%. The coupling efficiency at the trough of the oscillation is considerably high. For example, at an overlapping length of 70 μm, where the coupling efficiency is very close to the trough, the coupling efficiency from silica microfiber to PVA fiber is 83.6%, and from PVA fibers to silica microfibers is 82.6%. This behavior is clearly illustrated in Fig. 5(b) and (c). A substantial amount of energy is transferred from silica microfiber to PVA fiber, and vice versa, resulting in a high coupling efficiency.

III. Sensor Fabrication and Experimental Results

In the hybrid plasmonic waveguide structure as shown in Fig. 1, the Au film with a thickness of 500 nm was fabricated by electron-beam evaporation. The photoresist layer (Zep 520) was then spin-coated on the surface of the Au film. The grating pattern on the photoresist layer was formed through e-beam lithography. After these, the metal grating could be achieved using ion-beam etching with the photoresist acting as the soft mask for etching. Finally, using acetone and N-Methyl-2-Pyrrolidinone

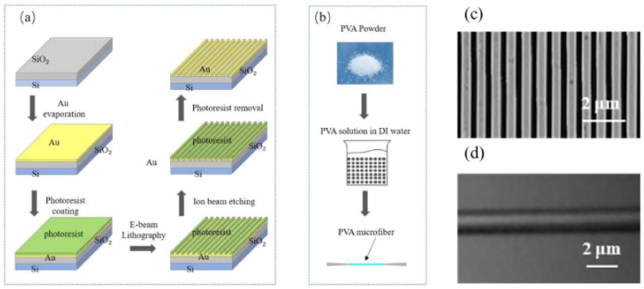

Fig. 6. (a), (b) Fabrication processes of the metal grating and PVA microfiber, respectively and (c), (d) SEM images of the metal grating and PVA microfiber, respectively.

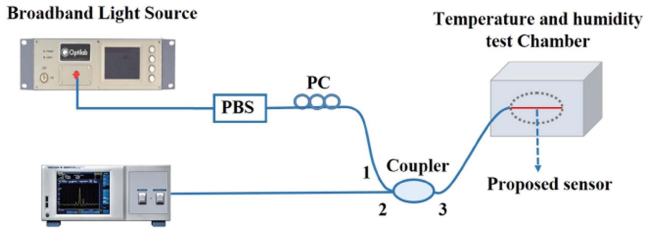

Fig. 7. Schematic diagram of the experimental setup for relative humidity and temperature measurement.

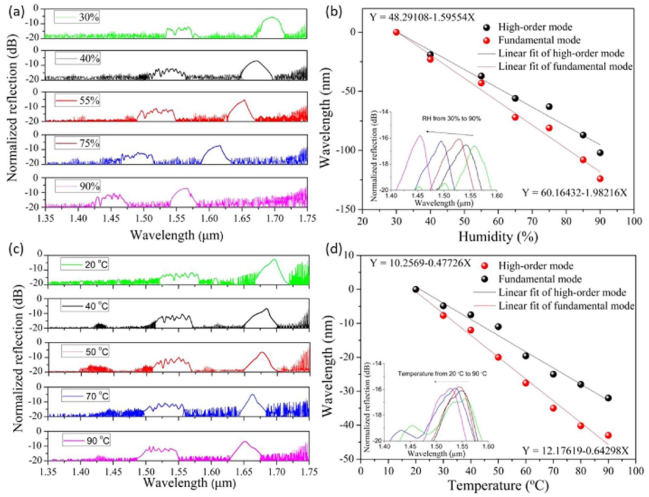

Fig. 8. (a) Measured TM reflection spectra for different RH. (b) Wavelength shifts of the fundamental mode and high-order mode versus the RH change. Inset displays shifts of high-order mode wavelengths after being performed a process of Savitzky-Golay smoothing. (c) Measured TM reflection spectra for different temperatures. (d) Wavelength shifts of the fundamental mode and high-order mode versus temperature change. Inset displays shifts of high-order mode wavelengths after being performed a process of Savitzky-Golay smoothing.

to clear the remained photoresist, the hybrid waveguide Bragg grating was obtained. The process is shown in Fig. 6(a).

In the experiments, the preparation of PVA microfiber is shown in Fig. 6(b). Deionized water and PVA particles (1788, from Aladdin) were mixed in a 100 ml glass beaker at a mass ratio of 2.5:1. To fully dissolve PVA particles, continuously stir with a glass rod for 30 minutes while heating the solution to 95 °C. Cool the uniformly dissolved PVA solution to room temperature and place it in an ultrasonic device to remove bubbles from the PVA solution. Freeze the PVA solution after removing bubbles in a low-temperature chamber (−5 °C–20 °C) for 12 hours. Slowly pull out PVA microfibers using a tungsten needle tip after thawing the frozen mixture at room temperature for 1 hour. The two ends of the PVA microfiber were coupled with adiabatic SMF tapers drawn by the flame heating technique [20]. The diameter of the SMF taper varied from several microns to submicrometers in the direction of tapering, ensuring a good match between the mode field diameter of a PVA microfiber and that of SMF tapers, resulting in efficient coupling [21]. The PVA microfiber with its two ends connected with SMF tapers was held in place by two translation stages, while the Au grating was fixed on another translation stage and positioned directly underneath the PVA microfiber. By adjusting the translation stage at one end of the PVA microfiber, the fiber gradually bent and made contact with the Au grating. Due to Van der Waals forces, the PVA microfiber tightly adhered to the metal grating as soon as it contacted the grating. Fig. 6(c) and (d) show the scanning electron micrograph images of the PVA microfiber and Au grating, respectively. The measurement shows that the diameter of PVA microfiber was ∼1.57 μm, the grating period was approximately ∼650 nm, the width of the air slit was ∼260 nm. The contact length and angle between PVA microfiber and grating were about 1 mm and 0°, respectively.

Fig. 7 shows the schematic diagram of the experimental setup for humidity and temperature measurement based on the HPWBG sensor structure (see Fig. 1). During the test of RH and temperature, the sensor was placed in a precise Temperature and Humidity Test chamber. A broadband light source was employed, with the output light being polarized using a polarization beam splitter(PBS). Subsequently, a polarization controller(PC) was utilized to adjust the light to TM polarization prior to entering the sensor. An optical spectrum analyzer was utilized to record the reflection spectra. A 3-dB coupler was placed ahead of the sensor to separate the reflected light.

Humidity measurements were performed when the RH was changed from 30 to 90% RH at room temperature of 20 °C. Fig. 8(a) illustrates the recorded reflection spectra of the hybrid Bragg grating under different humidity of 30, 40, 55, 75, and 90% RH. A noticeable shift towards shorter wavelength is observed in the reflection bands of both the fundamental mode and the higher order mode. It should be noted that the reflection spectra of higher-order mode exhibit irregularities due to undesirable noise. In order to minimize the noise, a Savitzky-Golay smoothing process was carried out, as depicted in Fig. 8(b) (inset). Fig. 8(b) gives the wavelength of λ_{Bf} and λ_{Bh} as a function of RH. When RH increases from 30% to 90%, the fundamental mode blue-shifts from 1697.09 nm to 1567.19 nm and the high-order mode blue-shifts from 1555.79 nm to 1454.15 nm. The RH sensitivities of the fundamental mode and high-order mode are −1.98 nm/%RH and −1.60 nm/%RH, respectively, obtained by linear fitting.

In the temperature experiment, the temperature is set from 20 °C to 90 °C while maintaining the RH at 30%. As depicted in Fig. 8(c), the fundamental mode exhibits a total blue-shift of

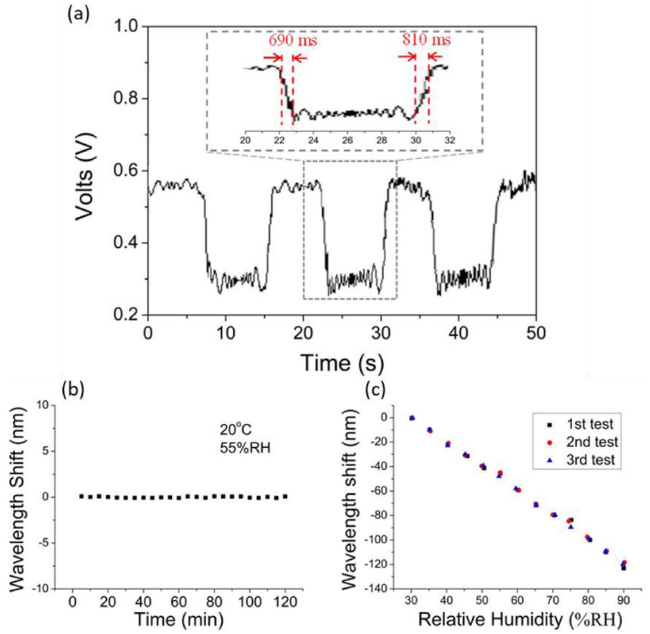

Fig. 9. (a) Time response of the RH sensor. (b) The fluctuation of reflected wavelength while keeping the temperature and relative humidity constant at 25 °C and 55%. (c) Reflected wavelength shift of the fundamental mode with increasing RH for the senor, 3 tests over a span of 7 days were conducted.

approximately 43.09 nm, and the high-order mode experiences a total blue-shift of around 31.7 nm. Fig. 8(d) demonstrates the relationship between temperature fluctuations and wavelength shifts of the fundamental mode and high-order mode. The inset of Fig. 8(d) shows the high-order mode wavelengths after being performed a process of Savitzky-Golay smoothing. The sensitivities of the fundamental mode and high-order mode are -0.64 nm/°C and -0.48 nm/°C, respectively.

The coefficient matrix enables the differentiation between changes in RH and temperature, as indicated by (2). By substituting the RH sensitivities and temperature sensitivities of λ_{Bf} and λ_{Bh} into (2), we can obtain

$$\begin{bmatrix} \Delta T \\ \Delta RH \end{bmatrix} = \frac{1}{0.0799} \begin{bmatrix} -1.59554 & 1.98216 \\ 0.47726 & -0.64298 \end{bmatrix} \begin{bmatrix} \Delta\lambda_{Bf} \\ \Delta\lambda_{Bh} \end{bmatrix} \quad (3)$$

Time response testing of the RH senor is important for evaluating its performance. A tunable laser was tuned at 1654 nm, close to the peak wavelength of the fundamental mode when the sensor is placed in the air at 20 °C (see Fig. 8(a)). The ambient humidity during the test was ∼55%RH. A periodic wet/dry air was imposed on the sensor under control to achieve a sudden humidity change, similar to the method mentioned in reference [16]. The RH of humid air was ∼90%. An electrical oscilloscope was used to detect the variation in light power through a PD during the process of continuously and repeatedly turning on and shutting off the humid air. As depicted in Fig. 9(a), the sensor underwent dynamic testing for three consecutive humidity switch cycles. Rise time and fall time (10% base line to 90% signal maximum) were estimated as 690 ms and 810 ms, respectively.

TABLE I
COMPARISON OF DUAL-PARAMETER SENSING PERFORMANCE BETWEEN DIFFERENT FIBER STRUCTURE SENSORS

Fiber Structure	RH sensitivity & range	Temperature sensitivity & range	Response Time	Resolution
PC [13]	129 pm/%RH (40-90%RH)	0.043 nm/°C (30-100°C)	0.3s	-
FPI [16]	-23.1 pm/%RH (30- 90%RH)	-6.14 pm/°C (10-50°C)	0.66s	±0.04%RH
U-shaped [17]	0.21 nm/%RH (20-75%RH)	-0.19 nm/°C (30-50°C)	0.54s	-
HPWBG in this work	-1.98 nm/%RH (30-90%RH)	-0.64 nm/°C (20-90°C)	0.69s	±0.04%RH

To further analyze its sensing capabilities, stability and repeatability tests were conducted on the proposed sensor. Fig. 9(b) demonstrate the variations in wavelength shift of the fundamental mode after the sensor was kept at 20 °C and 55%RH for duration of 2 hours. The data was recorded every 5 minutes. The fluctuations of power change and wavelength shift are within ±0.089 nm, which means a relative good stability of our sensor. According to Fig. 9(b), the standard deviation in detecting the power change and the wavelength shift can be calculated as 0.0713 nm. As a result, the RH detection resolution is determined to be ±0.04%RH. To assess repeatability, three sets of measurements were conducted on days 1, 3, and 5 over the course of a week. During the humidity test, the humidity was increased from 30% to 90% at 20 °C. As shown in Fig. 9(c), the performance is stable over repeated measurements with small standard errors at each RH reading.

Table I list several types of humidity and temperature sensors with different fiber structures including PC, U-shaped microfibers, FPI, and HPWBG. Compared to the sensors in [13], [16], [17], that detect humidity and temperature simultaneously, the sensor developed in this study exhibits enhanced sensitivity in both humidity and temperature. The sensitivity of RH is slightly below that in [14], [15], however, the temperature influence during RH tests of our sensor can be eliminated.

IV. CONCLUSION

In this article, we propose and demonstrate a HPWBG consisting of a PVA microfiber placed on an array of metal strips. The device enables the simultaneous measurement of RH and temperature. The sensor offers a sensitivity of -1.98 nm/%RH for humidity measurement within the 30–90% humidity range and shows a sensitivity of -0.64 nm/°C for temperature measurement within the 20–90 °C temperature range. The capability to measure RH and temperature simultaneously, along with its high sensitivity, excellent repeatability, rapid response, and the flexibility in construction make the proposed hybrid waveguide as a promising sensor for high-accuracy RH measurement.

REFERENCES

[1] D. L. Presti, C. Massaroni, and E. Schena, "Optical Fiber gratings for humidity measurements: A review," *IEEE Sensors J.*, vol. 18, no. 22, pp. 9065–9074, Nov. 2018, doi: 10.1109/jsen.2018.2870585.

[2] C. Shen et al., "Spatializing the roughness length of heterogeneous urban underlying surfaces to improve the WRF simulation-part 1: A review of morphological methods and model evaluation," *Atmospheric Environ.*, vol. 270, 2022, Art. no. 118874, doi: 10.1016/j.atmosenv.2021.118874.

[3] S. Khan, M. A. A. Mohammed, A. Rahman, and I. Hussain, "Optimization of Meteorological Monitoring Network of New South Wales, Australia," *Water Resour. Manage.*, vol. 37, no. 9, pp. 3395–3419, Jul. 2023, doi: 10.1007/s11269-023-03507-y.

[4] E. Padoan, J. Maffia, P. Balsari, F. Ajmone-Marsan, and E. Dinuccio, " Soil PM10 emission potential under specific mechanical stress and particles characteristics," *Sci. Total Environ.*, vol. 779, Jul. 2021, Art. no. 146468.

[5] W. Zhang et al., "Advances in tapered optical Fiber sensor structures: From conventional to novel and emerging," *Biosensors-Basel*, vol. 13, no. 6, Jun. 2023, Art. no. 644.

[6] M. N. Zahid, J. L. Jiang, and S. Rizvi, "Reflectometric and interferometric fiber optic sensor's principles and applications," *Front. Optoelectron.*, vol. 12, no. 2, pp. 215–226, Jun. 2019, doi: 10.1007/s12200-019-0824-6.

[7] R. J. He, C. X. Teng, S. Kumar, C. Marques, and R. Min, "Polymer Optical Fiber liquid level sensor: A review," *IEEE Sensors J.*, vol. 22, no. 2, pp. 1081–1091, Jan. 2022, doi: 10.1109/JSEN.2021.3132098.

[8] J. D. Hou, J. X. Dai, F. Zhang, and M. H. Yang, "Advanced Fiber-optic relative humidity sensor based on graphene quantum dots doped polyimide coating," *IEEE Photon. Technol. Lett.*, vol. 34, no. 14, pp. 725–728, Jul. 2022, doi: 10.1109/LPT.2022.3181756.

[9] Y. Y. Wang, J. Lin, L. N. Guo, M. G. Tian, and F. L. Meng, "Development of fabrication technique and sensing performance of optical fiber humidity sensors in the most recent decade," *Measurement*, vol. 215, Jun. 2023, Art. no. 112888.

[10] N. Wang et al., "Optical Fiber fabry-perot humidity sensor filled with polyvinyl alcohol," *Sensors Mater.*, vol. 33, no. 3, pp. 1051–1062, Apr. 2021, doi: 10.18494/SAM.2021.3229.

[11] H. G. Guo et al., "Fiber humidity sensor based on SF-LiBr composite film," *IEEE Sensors J.*, vol. 22, no. 17, pp. 16886–16891, Sep. 2022, doi: 10.1109/JSEN.2022.3186001.

[12] X. Rao et al., "Review of optical humidity sensors," *Sensors*, vol. 21, no. 23, Dec. 2021, Art. no. 8049.

[13] C. Y. Zhao, Q. C. Yuan, L. Fang, X. T. Gan, and J. L. ZHAO, "High-performance humidity sensor based on a polyvinyl alcohol-coated photonic crystal cavity," *Opt. Lett.*, vol. 41, no. 23, pp. 5515–5518, Dec. 2016, doi: 10.1364/OL.41.005515.

[14] Y. Shao et al., "Mechanism and characteristics of humidity sensing with polyvinyl alcohol-coated Fiber surface plasmon resonance sensor," *Sensors*, vol. 18, no. 7, Jul. 2018, Art. no. 2029, doi: 10.3390/s18072029.

[15] Y. Wang, J. R. Wang, Y. Shao, C. R. Liao, and Y. P. Wang, "Highly sensitive surface plasmon resonance humidity sensor based on a polyvinyl-alcohol-coated polymer optical Fiber," *Biosensors*, vol. 11, no. 11, 2021, Art. no. 461, doi: 10.3390/BIOS11110461.

[16] S. N. Wu, G. F. Yan, A. G. Lian, X. Chen, B. Zhou, and S. L. He, "An open-cavity Fabry-Perot interferometer with PVA coating for simultaneous measurement of relative humidity and temperature," *Sensors Actuators B: Chem.*, vol. 225, pp. 50–56, Mar. 2016, doi: 10.1016/j.snb.2015.11.015.

[17] T. K. Chen, H. M. Jiang, H. Y. Xia, H. Z. Luo, and K. Xie, "U-shaped microfiber sensor coated with PVA nanofibers for the simultaneous measurement of humidity and temperature," *Sensors Actuators: B. Chem..*, vol. 378, Dec. 2023, Art. no. 133203.

[18] K. O. Hill and G. Meltz, "Fiber Bragg grating technology fundamentals and overview," *J. Lightw. Technol.*, vol. 15, no. 8, pp. 1263–1276, Aug. 1997, doi: 10.1109/50.618320.

[19] Z. R. Tong, P. P. Luan, Y. Cao, W. H. Zhang, and J. Su, "Dual-parameter optical fiber sensor based on concatenated down-taper and multimode fiber," *Opt. Commun.*, vol. 358, pp. 77–81, Apr. 2016, doi: 10.1016/j.optcom.2015.09.027.

[20] J. Y. Lou, Y. P. Wang, and L. M. Tong, "Microfiber optical sensors: A review," *Sensors*, vol. 14, no. 4, pp. 5823–5844, Apr. 2014, doi: 10.3390/s140405823.

[21] W. H. Long, W. W. Zou, X. W. Li, and J. P. Chen, "DNA optical nanofibers: Preparation and characterization," *Opt. Exp.*, vol. 20, no. 16, pp. 18188–18193, Jul. 2012, doi: 10.1364/OE.20.018188.